

Modelling electron-induced processes in “condensed” formic acid

Resonant states of $(\text{HCOOH})_2^-$ at low energies

F.A. Gianturco^{1,a}, R.R. Lucchese², J. Langer³, I. Martin³, M. Stano³, G. Karwasz³, and E. Illenberger³

¹ Department of Chemistry, University of Rome La Sapienza, Piazzale A. Moro 5, 00185 Rome, Italy

² Department of Chemistry, Texas A & M University, College Station, Texas 77843-3255, USA

³ Institut für Chemie-Physikalische und Theoretische Chemie, Freie Universität Berlin, Takustraße 3, 14195 Berlin, Germany

Received 11 April 2005 / Received in final form 6 June 2005

Published online 23 August 2005 – © EDP Sciences, Società Italiana di Fisica, Springer-Verlag 2005

Abstract. Quantum calculations and experiments with molecular beams have been carried out for the Formic Acid dimeric structures colliding with a beam of slow (<20 eV) electrons. The corresponding computed S -matrix poles, seen as signatures for the formation of transient negative ions, allow us to assign the resonances to specific doorway states which are suggested to be responsible for the fragmentation patterns observed in the present experiments and in earlier measurements carried out both in molecular beams and with films of formic acid. We further show the computed behaviour of partial cross-sections and partial eigenphase sums for the dominant symmetry components.

PACS. 34.80.Bm Elastic scattering of electrons by atoms and molecules – 34.80.Gs Molecular excitation and ionization by electron impact

1 Introduction

The formic acid dimer, a prototype of carboxylic acid dimers, is one of the most stable neutral complexes for which the estimated formation energy is ~ 15 kcal mol⁻¹ [1]. It is, in fact, known to form as its ground-state structure a cyclic eight-membered ring with two O–H \cdots O hydrogen bonds [1]. Recent theoretical [2] and experimental [3,4] studies on the dimer have further analyzed in great detail the landscape of its multidimensional (Born-Oppenheimer) potential energy surface and of its special features, thereby confirming the presence of the above as the lowest energy structure, but also indicating an interesting set of similar but different dimeric structures of the complex located not far in energy.

Because of the obvious importance of hydrogen bonds in biology and chemistry, the presence of double hydrogen bonds has been found to play a critical role and to serve as a model system for the understanding of DNA base pairs. Multiple proton transfer in H-bonded species is indeed one of the fundamental molecular mechanisms in biology, as it governs oxidation-reduction steps in many reactions, whereby catalytic effects in enzymes can then be viewed as occurring via vibrationally-enhanced proton transfer mechanisms [5,6].

The corresponding monomer (HCOOH) is also of great importance in the analysis of the spectral signals which

originate from the interstellar medium [7] and have led to the suggestion that the monomer, and perhaps even the dimer, could be considered as key compounds in the formation of small biomolecules as the building blocks of larger molecular structures of biological interest in the early universe [8].

It is therefore of current interest to try and see what would be the role of (HCOOH) and of the formic acid dimer (FAD), at the molecular level, in the various intermediate species which are expected to be produced by radiation damage initiated by secondary electrons in condensed-phase and gas-phase molecular biosystems [9]. The further fact that recent studies on the structure of FAD in helium nanodroplets [4] have suggested the presence of non-cyclic polar structures dominated by long-range dipole-dipole forces as additionally possible (together with the lowest-energy, stable cyclic structure), makes it likely to have to consider the FAD to be an important structural fixture in the study of condensed species which are formed by deposition on cryogenically cooled monocrystals [10]. In other words, it is conceivable to employ the FAD species as a model system for the description of the dominant structures which occur on a film-deposited formic acid sample. The latter situation represents the “condensed-phase” of our title system that has been experimentally studied by electron-impact measurements. The previous studies of the gas-phase monomeric species [11] by electron scattering at low energies, and the corresponding theoretical analysis

^a e-mail: fa.gianturco@caspur.it

of the possible fragmentation-causing transient, resonant species [12], have turned out to be in very good accord with each other, hence suggesting that a further study of the more recent, condensed-phase experiments could also be profitably analyzed through the same type of computational models.

A comparison between calculations and experimental findings is particularly interesting for the case of gas phase clusters. While desorption from condensed phase formic acid (FA) is subjected to specific energy constraints (only those fragment ions are detected which gain sufficient translational energy to overcome the energy barrier due to polarization), electron attachment to clusters gives access to the full variety of charged species arising from the dissociative electron attachment (DEA) reaction in aggregated FA. In very recent work by the Berlin group [13] it was demonstrated that in the negative ion mass spectrum of FA clusters (generated in a supersonic expansion) the dimer anion (FAD^-) and its dehydrogenated form (FAD-H^-) are the predominant products formed at an electron energy near 1 eV. In the following section we shall therefore show ion yield curves of these ions detected at 92 amu (M_2^-) and at 91 amu ($\text{M}_2\text{-H}^-$): such results are explicitly recorded and reported for the first time in the present work. Section 3 will then discuss our theoretical and computational modelling of the DEA processes, while Section 4 will compare the calculations with the experimental findings. Section 5 will finally summarize our conclusions.

2 Experimental findings

The actual experimental data are shown by Figure 1, where we report on the upper panel the spectrum at 91 amu due to the $(\text{FAD-H})^-$ ion, and in the lower panel the same feature but associated with the $(\text{FAD})^-$ species at 92 amu.

One clearly sees that the resonances due to the two species of Figure 1 are appreciably broader than those seen before for the monomer $(\text{FA-H})^-$ [11], with the experimental appearance energy close to 0 eV. A further observation is that $(\text{FAD-H})^-$ at 91 amu shows pronounced features at higher energies which are not present on the $(\text{FAD})^-$ ion yield at 92 amu. In the present experiment we do not know a priori the identity (size) of the target cluster from which the particular ion under observation is formed. It is, however, likely that most of the intensity of $(\text{FAD-H})^-$ signal at 91 amu arises from initial attachment events to larger clusters. This is a common situation in electron attachment to clusters and a consequence of the available pathways to dissipate energy. Electron attachment to FAD may not form an anion $(\text{FAD})^-$ which is observable on the mass spectrometric time scale due to the lack of effective mechanisms to stabilize $(\text{FAD})^-$ anion by evaporation of the neutral components (evaporative electron attachment) [14]. In contrast to that, the ion $(\text{FAD-H})^-$ arises from the breaking of a chemical bond which requires appreciable energy so that the overall DEA process at the dimer is expected to be slightly endother-

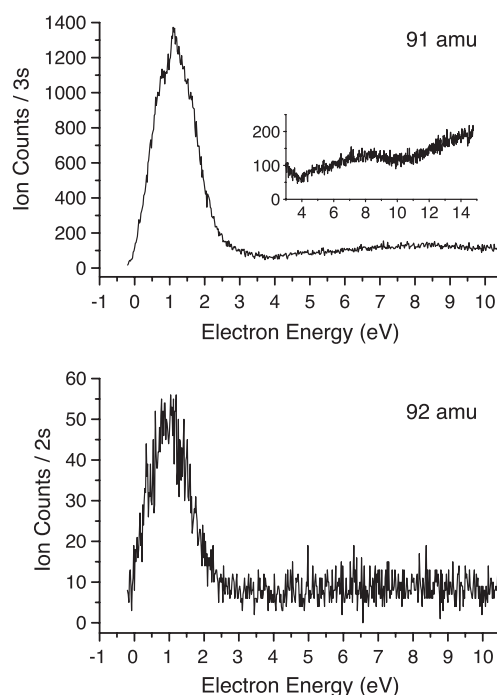


Fig. 1. Upper panel: ion yield curve for the $(\text{FAD-H})^-$ signal at 91 amu observed from electron attachment to a beam of neutral clusters formed by adiabatic expansion of formic acid seeded in He. Lower panel: ion yield curve for $(\text{FAD})^-$ ion yield at 92 amu observed under the same conditions as those in the upper panel.

mic. We can hence assume that most of the $(\text{FAD-H})^-$ ions arise from electron attachment to neutral dimers.

It should be noted that we shall definitely assign the features observed at higher energies on the $(\text{FAD-H})^-$ signal at 91 amu to *resonances* and not to *inelastic scattering events*. Only in clusters consisting of molecules with high attachment cross-sections at 0 eV, features at higher energies may also arise from inelastic scattering events (e.g. see a more extensive discussion of this point in Ref. [14]). In that case, the incoming fast electron in the first step generates an electronically excited molecule in the cluster, and in the second step the slowed down electron (0 eV) is captured by a second molecule of the same cluster. Since FA is a comparatively weak electron scavenger with the cross-section maximum distinctly off the threshold of 0 eV, the features at higher energy cannot arise from inelastic electron scattering events.

3 The dynamical model: an outline

To gain a physical picture at the molecular level of the initial effects of slow-electrons impacting on the present species we need to know first the interaction potentials which will act during that event and then use them within a quantum formulation of the scattering process. We draw now on our earlier, extensive experience [15] in treating electron scattering processes off polyatomic targets in the

gas phase and provide here only a brief outline of our theoretical models, referring the reader to one of our previous reviews for further details [16].

3.1 The scattering equations

Within the Born-Oppenheimer (BO) scheme the total wave function of a continuum electron scattered from an N -electron molecular target is an antisymmetrized product of one-electron orbitals that parametrically depend on the nuclear coordinates: our present treatment shall be limited to the elastic channels and no excitations will be considered for either the bound electrons or the bound nuclei. In fact, we will describe the scattering within the fixed-nuclei (FN) approximation [17], which neglects any dynamics involving the nuclear motion, whereas the bound electrons will be taken to be in the ground electronic state of the target at its optimized nuclear geometry. The initial description of that state will be given as a single-determinant of near-Hartree-Fock molecular orbitals (MOs) of the N -bound electrons. To obtain our scattering equations we then expand both the bound MOs and the continuum electron in a single-center (SCE) at the center of mass of the target by employing symmetry-adapted angular functions for each of the irreducible representations (IRs) that belong to the molecular point-group at the chosen geometry

$$F^{p\mu}(r, \hat{\mathbf{r}}|\mathbf{R}) = \sum_{l,h} r^{-1} f_{lh}^{p\mu}(r|\mathbf{R}) X_{lh}^{p\mu}(\hat{\mathbf{r}}). \quad (1)$$

The indices refer to the μ th element of the p th IR of the point group of the complex (C_{2h} in the present case) at the geometry \mathbf{R} . The angular functions $X_{lh}^{p\mu}(\hat{\mathbf{r}})$ are symmetry-adapted functions given by the proper combination of spherical harmonics $Y_{lm}(\hat{\mathbf{r}})$

$$X_{lh}^{p\mu}(\hat{\mathbf{r}}) = \sum_m b_{lmh}^{p\mu} Y_{lm}(\hat{\mathbf{r}}). \quad (2)$$

The coefficients $b_{lmh}^{p\mu}$ can be obtained from the character tables of the relevant molecular point group [18].

The coupled partial integro-differential scattering equations are

$$\left[\frac{d^2}{dr^2} - \frac{l(l+1)}{r^2} + 2(E - \epsilon_\alpha) \right] f_{lh}^{p\mu\alpha}(r|\mathbf{R}) = 2 \sum_{l'h'\mu'\beta} \int dr' V_{lh,l'h'}^{p\mu\alpha,p'\mu'\beta}(r,r'|\mathbf{R}) f_{l'h'}^{p'\mu'\beta}(r'|\mathbf{R}), \quad (3)$$

where E is the collision energy and ϵ_α is the electronic eigenvalue for the target ground state so that $(E - \epsilon_\alpha) = k^2/2$ where k is the asymptotic momentum of the scattered electron. The (p, μ) indices, equation (3), now label the specific μ th component of the p th IR that characterizes the continuum that belongs to the α th electronic target state (initial state) coupled with the excited states, labeled by β , with the corresponding continuum symmetry labeled by (p', μ') . If one now truncates the sum on the

right-hand side of equation (3) to a single state only, one obtains the exact-static-exchange (ESE) representation of the electron-molecule interaction for the ground state at the geometry \mathbf{R} . With the further assumption of having only a local e^- -molecule interaction (as we shall discuss below) one can write

$$\left[\frac{d^2}{dr^2} - \frac{l_i(l_i+1)}{r^2} + k^2 \right] f_i^{p\mu}(r|\mathbf{R}) = \sum_j V_{ij}^{p\mu}(r|\mathbf{R}) f_j^{p\mu}(r|\mathbf{R}), \quad (4)$$

where the indexes i , and j represent the “angular channel” (l, h) and the potential coupling elements are

$$V_{ij}^{p\mu}(r|\mathbf{R}) = \langle X_i^{p\mu}(\hat{\mathbf{r}}) | V(\mathbf{r}|\mathbf{R}) | X_j^{p\mu}(\hat{\mathbf{r}}) \rangle = \int d\hat{\mathbf{r}} X_i^{p\mu}(\hat{\mathbf{r}}) V(\mathbf{r}|\mathbf{R}) X_j^{p\mu}(\hat{\mathbf{r}}). \quad (5)$$

We have also replaced the exact operator of equation (3) with an energy-dependent local exchange potential [19]

$$V_{\text{ex}}^{\text{FEGE}}(\mathbf{r}) = \frac{2}{\pi} k_F(\mathbf{r}) \left(\frac{1}{2} + \frac{1 - \eta^2}{4\eta} \ln \left| \frac{1 + \eta}{1 - \eta} \right| \right), \quad (6)$$

where $\eta(\mathbf{r}) = (k^2 + 2I_p + k_F(\mathbf{r}))^{1/2}/k_F(\mathbf{r})$, $k_F(\mathbf{r}) = (3\pi^2\rho(\mathbf{r}))^{1/3}$ is the local Fermi momentum and I_p is the ionization potential of the molecular target.

When one restricts the summation in equation (3) to a single state, one excludes also possible virtual excitations of bound electrons, i.e. the effects of static and dynamic electron-electron correlation are neglected. The latter effects asymptotically produce the long-range multipolar polarization contributions which are of prime importance for low-energy electron scattering processes. We therefore include a modeling of the dynamical short-range correlation through the addition of a local energy-independent potential V_{corr} : it is obtained by defining an average dynamical correlation energy of a single electron within the formalism of the Kohn and Sham variational scheme [20]. The functional derivative of such a quantity with respect to the SCF N -electron density of the molecular target provides a density functional description of the required short-range correlation term, this being an analytic function of the target ground state electron density.

3.2 The adiabatic potential model

To examine in some detail the mechanism and qualitative characteristics of low-energy, one-electron resonances, we shall use a model simple enough to be computationally attractive but with sufficient details of the full scattering problem to reproduce the essential features of realistic cases. Thus, we employ a simple, purely local model potential we have called the static model exchange correlation (SMEC) potential, V_{SMEC} [15] which we already used to study the FA fragmentation data [12].

We start by noting that the standard, symmetry-adapted angular momentum eigenstates, $X_{lh}^{p\mu}$, do not form the most compact angular set for the electron-molecule scattering problem: an alternative expansion basis is provided by diagonalizing the angular Hamiltonian at each radius r . These new angular eigenstates are the adiabatic angular functions (AAFs) $Z_k^{p\mu}(\theta, \phi, r)$ which are r -dependent, linear combinations of the symmetry-adapted ‘‘asymptotic’’ harmonics

$$Z_k^{p\mu}(\theta, \phi, r) = \sum_{lh} X_{lh}^{p\mu}(\theta, \phi) C_{lh,k}(r), \quad (7)$$

where the expansion coefficients come from the matrix eigenvalue equation

$$\sum_{lh} V_{l'h',lh}(r) C_{lh,k}(r) = C_{l'h',k}(r) V_k^A(r). \quad (8)$$

The eigenvalues $V_k^A(r)$ now form an adiabatic radial potential for each index value k over the selected range of the e^- -molecule distance.

To solve the scattering equations with the adiabatic potential, actually approximate the adiabatic potential by a piecewise diabatic (PD) representation for the potential [12,15], where the radial coordinate is divided into many regions so that sector i is defined as $r_{i-1} < r < r_i$, with $r_0 = 0$. In each region, we average the coupling potential $V_{l'h',lh}(r)$ over r and the resulting averaged potential is diagonalized as in equation (8) to yield a set of angular functions $Z_{k,i}^{p\mu}(\theta, \phi)$. Then in region i the scattering potential is transformed into the new representation in which it is nearly diagonal. The resulting equations are then solved using the full scattering potential in each region with the further approximation of ignoring the off-diagonal couplings within each of the regions. The carrying of the radial functions from one region to the next is given by the transformation matrix $U_{k,k'}^{(i+1 \leftarrow i)}$ defined by

$$U_{k,k'}^{(i+1 \leftarrow i)} = \sum_{lh} C_{lh,k}^{(i+1)} C_{lh,k'}^{(i)}. \quad (9)$$

We accomplish the unitarization of $U_{k,k'}^{(i+1 \leftarrow i)}$ using simple Graham-Schmidt orthonormalization on the columns of $U_{k,k'}^{(i+1 \leftarrow i)}$.

The scattering was then solved within the reduced basis of the effective diabatic potential terms and the corresponding poles of the S -matrix have been obtained using a very narrow grid of values that however span the energy range of experimental interest, i.e. from threshold to about 20 eV. It is the structure of such poles in the complex plane that shall guide us in the search of resonances for our title system. Once they are located from the pole structure, however, we repeat the cross-section calculation in the vicinity of the poles and further analyse the computed eigenphase sums in that energy region [17].

Table 1. Computed shape resonances and virtual states for the FAD target complex. Energies and widths are in eV units of energy.

Symmetry	Virtual state	E_r/Γ_r	E_r/Γ_r
B_u	–	–0.09/1.18	–
A_u	–	2.87/0.66	–
B_g	–	3.68/0.60	–
A_g	–0.68	9.92/2.14	14.05/3.68
B_u	–	11.71/3.35	13.99/2.12

4 Discussion of results

4.1 The computational details

The geometry which we have employed for the target FAD is the one associated to its eight-atom ring with two H-bonded structures, and the relative bond distances and angles were those given by reference [2]. The basis set expansion used to generate the target wave function was the same we employed for the study on the HCOOH monomer in the gas-phase [12] (the aug-cc-pVTZ basis set). The radial integration region used to obtain the PD representation involved 100 sectors with an r_{\max} of 12.0 a.u., with the number of multipolar terms in the coupling potential of equation (5) going up to $l_{\max} = 40$. However, the number of terms employed within the PD representation of the full SMEC potential went up to $L_{\max} = 16$, the latter providing convergence of resonances locations and widths of a few percentage points. No asymptotic polarizability was added to the full interaction beyond the short-range effects of the V_{corr} discussed in the previous section. Since we are chiefly interested in the interaction range within which resonant states are formed, we did not deem necessary to also include such long-range effects [21].

The molecular symmetry of the FAD is now C_{2h} and we examined all the corresponding IRs, finding resonances in all the relevant symmetries: A_u , A_g , B_u and B_g . We found a total of eight resonances distributed over the above symmetries: one A_u , three A_g , one B_g and three B_u . Their energies and widths are given by Table 1. One should note here that the threshold B_u resonance yields a pole with a very small negative component on the real axis and a larger imaginary component which provides its decaying lifetime. Obviously scattering resonances must be in the positive energy continuum, although numerical searches of S -matrix poles can yield negative components on the real axis for threshold resonances as a numerical artifact of the search procedure: the physical result is still that of a resonance in the positive energy continuum since there is always a width associated to it.

Just to give a pictorial overview of the general behavior of the PD interaction representation for the four relevant IRs, we show in Figure 2 the lower contributing multipolar terms of the potentials.

One clearly sees in the figure that the range of electron energies up to about 20 eV, as we have considered here, chiefly interacts with the lower five or six contributing diabatic multipoles. However, our actual calculations

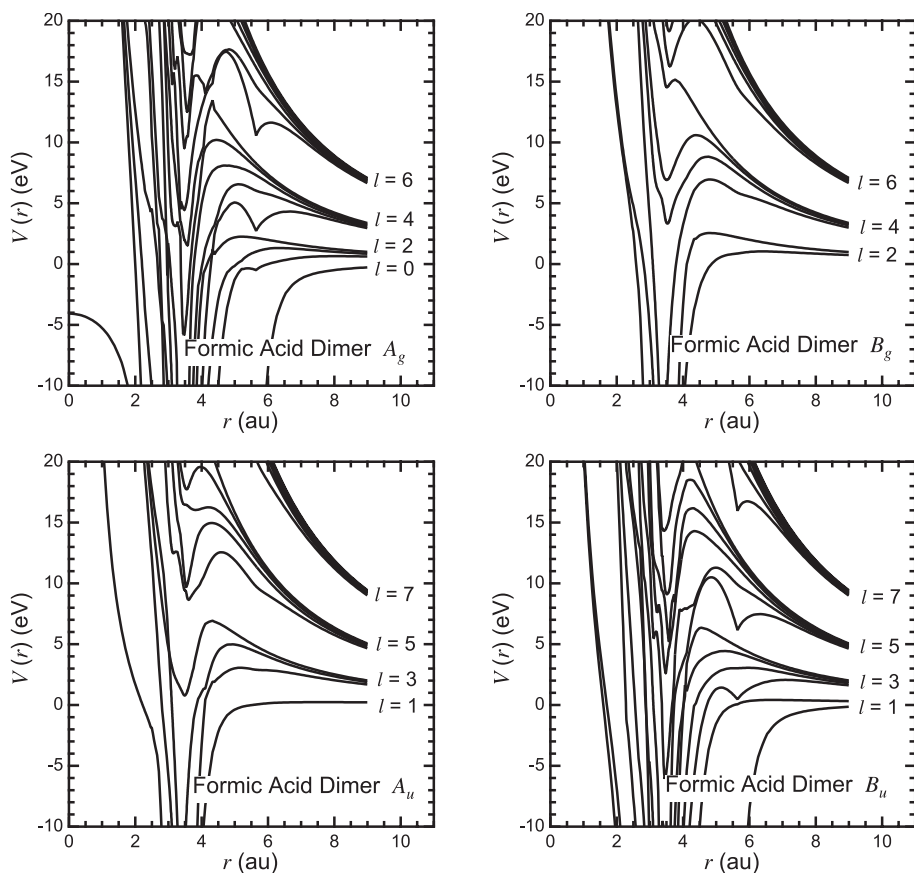


Fig. 2. Computed piecewise diabatic (PD) potential representation for the IRs contributing to the FAD symmetry components. Even values contribute to the A_g , B_g contributions, while odd potential values contribute to the A_u , B_u representations.

required L_{\max} up to 16 in order to reach numerical convergence for the cross-sections associated to the resonant features described in Table 1. We shall further see below that the dominant radial components of the resonant wave functions are also given at the most by two or three partial waves.

4.2 The earlier experimental data

Several experimental studies have been carried out in recent years on the electron attachment processes to a single FA molecule [11], to a film deposited five-monolayer sample of “condensed” FA [10] and to a series of its homogeneous clusters [13]. The earlier results on the single molecule [11], also confirmed by our present data and by the recent experiments [13], indicate that the monomer species in the gas-phase undergoes hydrogen abstraction via DEA and forms the closed-shell ion HCOO^- in the region of a low energy resonance centered around 1.25 eV. The findings on the clusters [20] further indicate that the DEA process is strongly enhanced and leads to a broader variety of transient negative ions (TNIs), among which the dimer $(\text{FA})_2^-$ and its dehydrogenated form, $(\text{FA})(\text{FA}-\text{H})^-$ are the most abundant [13]. Such species also appear present in the larger clusters as $(\text{FA})_n^-$ and $(\text{FA})_{n-1}(\text{FA}-\text{H})^-$.

The studies on the electron stimulated desorption from FA nanofilms showed [10] an intense H^- signal appearing

within a resonance structure that peaked around 9 eV, while the $(\text{FA}-\text{H})^-$ signal was markedly suppressed. The former reaction, therefore, is very different from that leading to hydrogen abstraction at much lower energies and should be related to a different transient structure of its TNI: our calculations below try to explain such differences at the molecular level.

The low-energy resonance associated with the hydrogen abstraction from the gas-phase monomer, $(\text{FA}-\text{H})^-$ [11] has also shown the H loss from the target molecule to occur from the O-H/O-D site of it, a feature also confirmed by our recent calculations on the gas-phase monomer [12]. Furthermore, our data on the clusters analysis from a supersonic molecular beam reported by Section 2 will indicate fairly clearly the presence of $(\text{FA})^-$, of $(\text{FAD}-\text{H})^-$ and of $(\text{FA}-\text{H})^-$ peaks from the DEA spectra collected at energies around 1 eV. In other words, the low-energy resonant features from experiments indicate the presence of TNIs where hydrogen abstraction can occur from both the dimer and the monomer, besides being present also in the larger clusters. Finally, the experiments on the clusters indicate the formation of the $(\text{FA})^-$ fragment which was not present in the electron attachment process occurring for the monomer molecule [13]. We shall see below that our calculations are also able to qualitatively rationalize such results by showing the formation of two specific resonance structures in the low-energy region.

Another suggestion from the experiments carried out on films [11] was that the hydrogen abstraction fragment

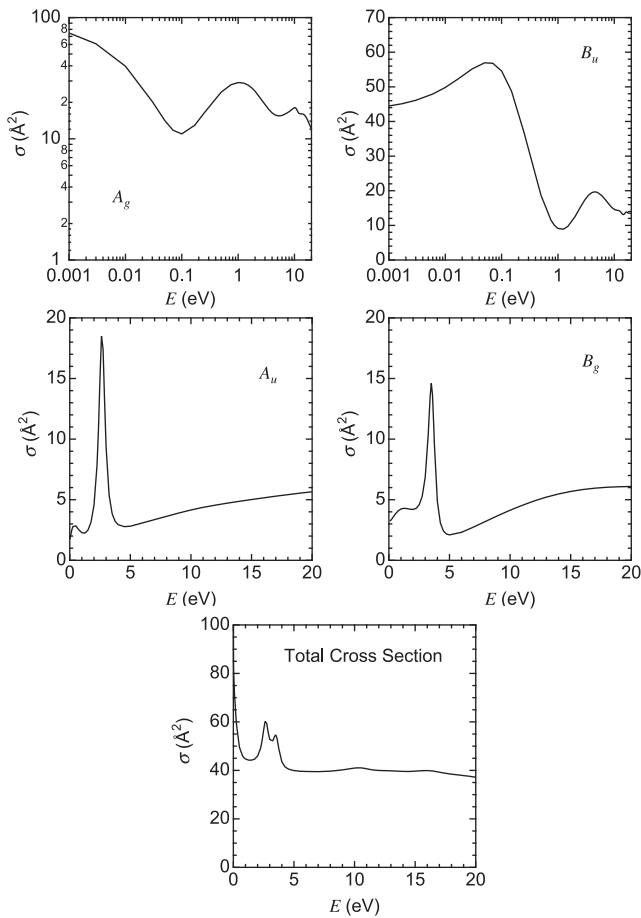


Fig. 3. Computed partial integral cross-sections of electron-FAD scattering for the four symmetry contributions where resonant features appear. The lowest panel at the center reports the total integral cross-sections. Energies are given in eV and cross-sections in \AA^2 .

(FA-H)⁻ is still possibly formed at low energies but does not leave the surface of the film as strong polarization forces are difficult to overcome: the calculations we presents here suggest that such species can indeed be formed from the gas-phase dimer.

Another, interesting set of information can be gathered from the experimental study of the spectra originating from the “condensed” FA deposited on a cryogenically cooled monocrystalline Au substrate [11] once the sample is irradiated for extended periods of time (up to 10 min of exposure time). The results suggest the presence of O⁻ signals in the energy range above 6 eV and CO₂ emission appearing from 12 eV and up to 20 eV of impinging electron energy, with the emission signal area steadily increasing above about 8 eV. These findings are also related to some of the resonant features which we found in our calculations, as we shall report in our following discussion.

4.3 Partial cross-sections and resonances

We report in Figure 3 the computed partial cross-sections for the four IRs contributing to the resonant features,

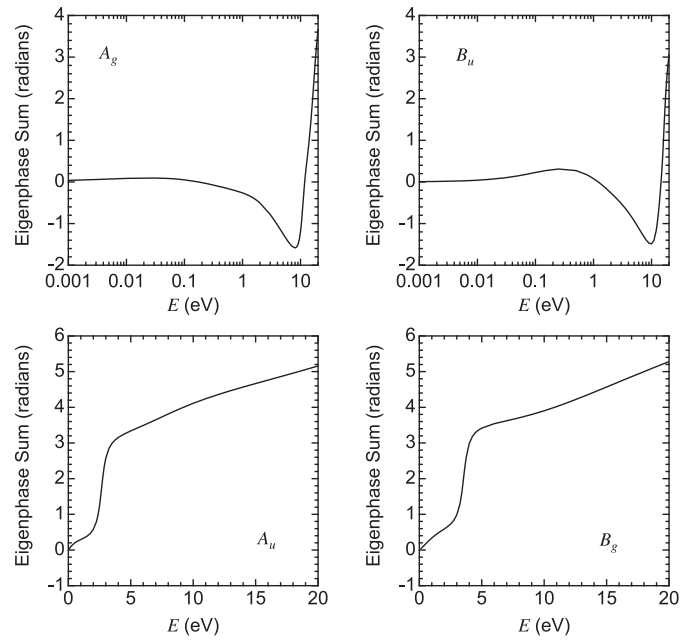


Fig. 4. Computed eigenphase sums for the four contributing symmetry of the FAD target. The units are radians.

together with the total, integral (rotationally summed) cross-section over the examined range of energies. One should note at the outset that, because of the highly non-spherical nature of the e^- -molecule interaction, each of the contributing IRs contain strong mixing of their contributing partial waves. Thus, even if each of them will show the dominance of its lowest partial wave at vanishing energies, such a behaviour occurs at much lower collision energies than those which we analyze in the present work.

One sees in Figure 3 the presence of one B_u symmetry resonance near threshold, two very strong resonances below 4 eV associated to the A_u and B_g symmetry components and another marked feature near threshold associated with the A_g resonance in that energy region. Furthermore, the A_g Irreducible Representation shows a marked resonance below 10 eV and another broad resonance further higher in energy. Likewise, the B_u contribution shows two additional, broad resonances above 10 eV. We have localized the A_g feature close to threshold as a virtual state (with dominant $l = 0$ component) and associated with a scattering length which is negative and large ($-4.5 a_0$) and which corresponds to a negative energy (-0.68 eV) pole in the unphysical Riemann’s sheet [17]. The various eigenphase sums are reported for all four IR contributions in Figure 4, confirm the presence of the threshold resonance of B_u symmetry, and of two marked resonances close to 3 eV coming from the A_u and B_g contributions. They further show the slowly increasing eigenphase sum of A_g symmetry as the energy goes to zero, a feature of the virtual state, a strong A_g resonance close to 9 eV, the threshold resonance of B_u symmetry and its further, broad resonances above 10 eV as we will discuss in more detail below. One should further note that a consequence of the negative scattering length is also related to the

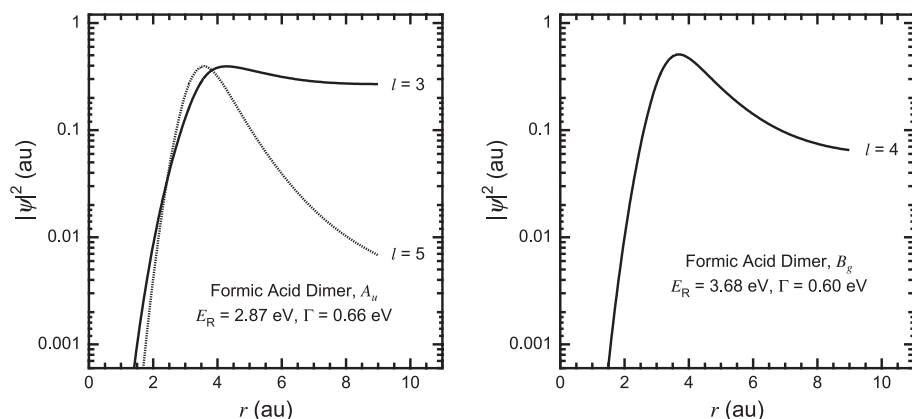


Fig. 5. Computed dominant radial components for the scattering probability densities associated to two low-energy resonances. Left panel: the A_u component; right panel: B_g component. Both distances and densities are in atomic units.

appearance of a Ramsauer-type minimum structure in the A_g component of Figure 3, although it is not to be expected that the total cross-section would clearly show its presence, as we can see in the bottom panel of Figure 3.

4.4 The very-low energy spectrum

We can analyze the spatial features of the low-energy resonances in order to relate their behavior to the experimental findings from both clusters spectra [13] and film depositions [11], where it has been surmised that electron-induced fragmentation patterns indicate the presence of FDA formation. We shall also relate them to the distinct spectra of Figure 1.

The observed threshold resonances are caused by electron trapping behind some specific potential barrier among those shown by the various contributing IRs potentials reported by Figure 2. We can therefore analyze the corresponding real radial components of the scattering wave functions or, more specifically, the probability densities associated to the dominant partial waves of such wave functions. The strong threshold resonance of B_u symmetry is dominated by the $l = 1$ component which creates the local trapping of the excess, metastable electron. However, since we are really discussing a multichannel situation and therefore we have several partial waves coupled by the molecular anisotropic potential, the $l = 1$ channel has sizeable nonadiabatic coupling with the $l = 0$ and $l = 2$ components. Hence, one can observe in some cases the appearance of an S -matrix pole associated with a resonance energetically located above the barrier of a given diabatic component. We therefore see here a resonance above the barrier due to nonspherical couplings to neighboring partial waves: it is, however, a fairly broad resonance and the trapped electron can easily escape from the molecule [15]. We shall discuss later on some of its more important spatial features. Furthermore, we report the other two low-energy resonances in Figure 5: on the left panel we show the two dominant radial components of the A_u resonance located at 2.87 eV by our model calculations, with a width of 0.66 eV. One clearly sees there that a very high angular momentum barrier, the $l = 5$ component, is trapping the excess electron on the central region of the dimer (the

center of mass is located on the central point between the two middle points of the H-bonds) while the decay occurs by non-adiabatic coupling with the $l = 3$ channel. The figure shows, in fact, that the $l = 3$ component describes an outgoing wave associated to TNI break-up.

The results for the B_g resonance, located at a slightly higher energy value of 3.68 eV (with a width of 0.60 eV), are reported on the right-side panel of the same figure. The picture for the dominant component of the radial density is even simpler: there is only one important partial wave that describes a trapped excess electron behind the $l = 4$ barrier. The density shows, in fact, the behavior of a “bound” state that decays chiefly by tunneling through the dominant barrier, i.e. a nearly one-potential picture of the system is able to describe the electron tapping for that resonant state.

The experiments on the low-energy region of the DEA fragmentation patterns from FA clusters [13] indicate the presence of $(FA)^-$ and $(FA-H)^-$ smaller fragments, together with a strong signal from $(FAD)^-$ and $(FAD-H)^-$ fragments, as those shown by the data of Figure 1 in the present work. In order to see whether we can extract such indications from our trapped resonance states, it is expedient to display their corresponding spatial features and nodal structure over the molecular network of the nuclei. The results of such an analysis are given by Figure 6 for the near-threshold B_u resonance and by Figure 7 for the next two resonances of A_u and B_g symmetries.

The threshold features shown by the cluster spectra of Figure 1 indicate the two resonances to be much broader than was the case for the monomer spectra [11] and cover an energy range of about 3 eV. Our calculations located three distinct resonances in that energy region and find the lowest one to be fairly broad, i.e. with a width of more than 1 eV.

The density map reported by Figure 6 indicates indeed excess electron density over the $-HCO_2^-$ fragments and also marked electron density values over and across the central H-bonded region. Thus, we can surmise that such a state corresponds to a precursor TNI that gives rise to the $(FAD)^-$ signal we observe experimentally in Figure 1.

If we now turn to the spatial structure of the nearby resonance of B_g symmetry (right panel of Fig. 7) we clearly see, on the other hand, the presence of a marked

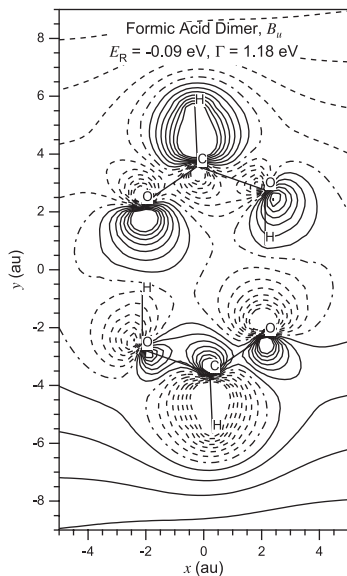


Fig. 6. Computed excess electron probability density mapped in the plane of the FAD. The density changes sign when going from the solid lines into the dashed ones.

antibonding plane cutting across the central H-bond network. The extra electron density is now absent on those H atoms and strongly localized on the $-\text{CO}_2^-$ parts of the FA monomers. We can therefore infer from such features that this resonant state is likely to undergo dissociative break-up into either of the monomers, which would give rise to the $(\text{FA})^-$ signal experimentally observed [20], or further undergo loss of one of the H atoms now freed from bonding, thereby producing an $(\text{FA}-\text{H})^-$ signal, also experimentally detected [13]. With the same token, we see that the nearby A_u resonance reported on the left panel of the same Figure 7, does not display marked antibonding feature across the H-bonds region, while still showing, however, no excess electron density over the “external” H atoms. Thus, we expect this metastable state to provide a precursor resonance that can lead to the $(\text{FAD}-\text{H})^-$ signal shown by the experiments recorded on the upper panel of Figure 1.

In conclusion, the analysis of our three resonant states at low energies (i.e. below 4 eV) indicates fairly strongly that their spatial distributions of the excess electrons can provide the necessary doorway states leading to the DEA fragmentation patterns which are experimentally observed. The energy positions, found by our calculations, are only qualitatively reproducing the resonance locations which we have seen in the experiments of Section 1. However, given the approximate nature of the present model, it is not surprising to find quantitative differences while it is reassuring to get from calculations a rather microscopic explanation of the DEA patterns observed experimentally.

We finally wish to note that the presence of near-threshold virtual state of A_g symmetry is indeed related to the strong threshold increase of the total cross-sections reported by the bottom panel of Figure 3. The corresponding eigenphase sum of Figure 4 indicates a slow rise as the

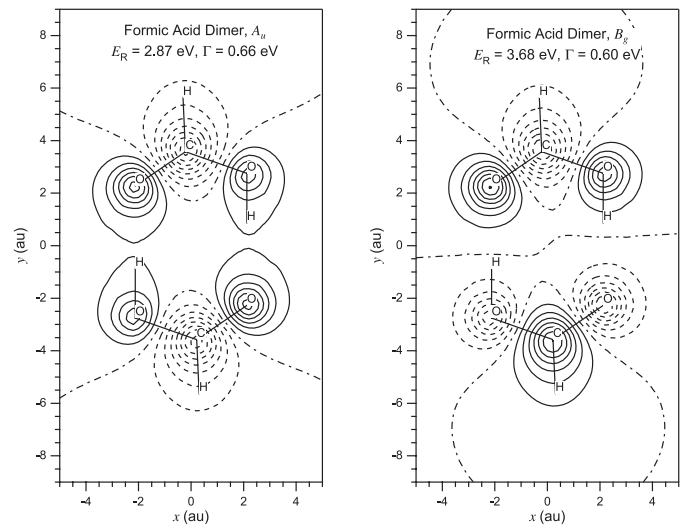


Fig. 7. Computed contours of the resonant wave functions associated with the A_u state (left panel) and the B_g state (right panel). The plots are given for a plane that is 0.75 au above the plane of the complex. The states represented here are π states so the the plane of the complex is a nodal plane. The solid lines and dotted lines correspond to different signs of the wave functions.

energy goes to zero, in accord with a virtual state formation which is however located slightly away from zero energy (-0.68 eV).

4.5 The H^- detachment region

The experiments on electron interactions with the monolayer of FA deposited on cryogenically cold monocrystalline Au substrate [10], i.e. with a target described as a sort of “condensed phase” FA, have shown the very marked presence of a broad resonance producing a strong H^-/D^- desorption signal that peaks around 9 eV. It also showed that the FAD species is very likely to be one of the components of the film polymerization process.

The present calculations on the FAD target have also uncovered a resonance around 9 eV (at 9.92 eV, in fact) which is broader than the ones at low energy discussed before ($\Gamma \sim 2$ eV) and which is of A_g symmetry. The radial component of the probability density for that scattering state are shown by Figure 8.

A greater number of the lower partial waves are now contributing to this resonance and therefore we expect its decaying efficiency to be somewhat higher, thereby causing its width to be larger, as observed both in our calculations and by the experiments (see Fig. 3 of Ref. [10]). In fact, the amplitudes of Figure 8 indicate the trapping process to occur behind the $l = 4$ potential curve but the decaying process to take place by couplings with the $l = 2$ and $l = 0$ components due to the anisotropy of the electron-molecule interaction. Furthermore, we see that the $l = 0$ and $l = 2$ components describe contributions to the scattering electron wave function that have their largest amplitudes around 1 and 2 au, respectively, from

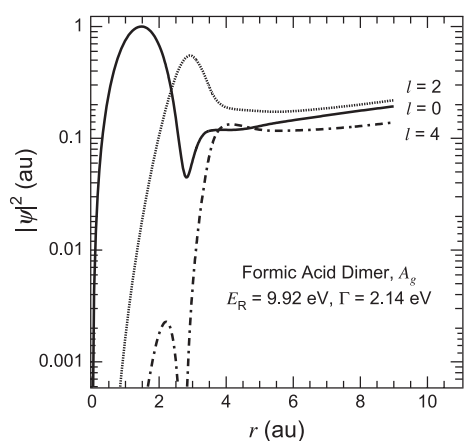


Fig. 8. Computed radial components (largest coefficients) of the TNI state of A_g symmetry at 9.92 eV. See text for details.

the expansion center. This means that the metastable, excess electron has its largest probability density chiefly located on the molecular spatial region that corresponds to the central H-bond network, as seen more clearly from the data of Figure 9: we report there the isolines for the wave function describing the resonant state of A_g symmetry. The features of that excess electron wave function allow us to note the following:

1. both the O–H and the O···H bonds show clearly the presence of antibonding features of the extra electron exactly across those bonds. On the other hand, contrary to what we saw for the lower-energy resonances, the extra electron density is clearly localized on the H atoms which form the dimer H-bonds. This means, at least qualitatively, that we expect the dimer species to be easily broken-up and further to be likely to lose the H atoms, but this time they will be with extra charge localized on them;
2. similar antibonding features are also seen to occur across the C–O bonds of C–O–H fragments, hence suggesting an additional pathway that could lead to FAD break up with the extra charge still located on one of the removed H atoms.

The features of this scattering wave function thus strongly indicate the possibility that this specific resonance can act as a precursor state to the DEA resonant fragmentation of the FAD at 9 eV with the production of H^- fragments.

4.6 The higher energy resonances

The experiments on electron scattering off the film deposited FA [10] have also discussed, as briefly summarized earlier, the possible reactions induced by extended electron irradiation. It was mentioned there that the extended exposure of the FA films indicated formation of CO_2 , and possibly of H_2O , at the surface and that the energy region over which such signals were detected started above 12 eV. A further O^- signal was also observed [10], starting from above 6 eV and extending up to 15 eV. All features are

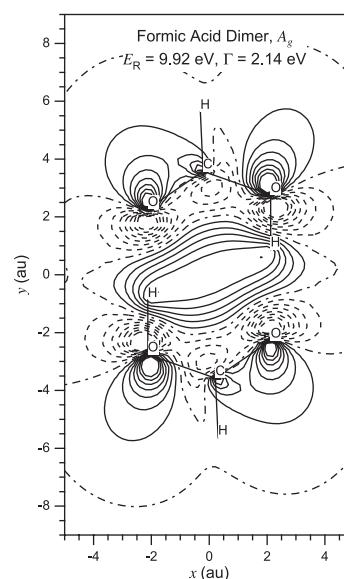


Fig. 9. Computed contours of the resonant state describing the A_g resonance of the FAD at 9.92 eV plotted in the plane of the complex. The changes of the line symbols correspond to opposite signs.

seen to be rather broad and to cover an extended range of energies.

Our present calculations further indicate the presence of three additional resonances above 11 eV and extending up to 14 eV. The radial coefficients for the corresponding resonance wave functions are given by Figure 10.

All three resonances show substantial contributions from several partial waves as reported in the figure. We therefore expect that the corresponding excess electron wave functions would exhibit a fairly complicated nodal pattern across several bonding regions. This is borne out by the density maps of Figure 11.

We see there that the CO_2 units of the FA partner molecules are carrying substantial excess electron charge and their bonding to both the other monomer and to the H atoms show marked antibonding features. Thus, we suggest that such resonances, e.g. see the ones shown by Figure 11 in the middle and right panels (the B_u resonance at 13.99 eV and the A_g resonance at 14.05 eV), could be considered as precursor states which are likely to decay following fairly complicated bond fragmentation paths that preserve the CO_2^- units while breaking up the dimer and causing H losses from the fragments.

By the same token, we again see that all three resonances, e.g. see specifically the one around 11.7 eV, indicate substantial extra electron charge to be located over the oxygen atoms partaking of the hydrogen bonding and of the O–H bonds. They could therefore also be the precursor states for which the FAD’s break up is followed by further bond-breaking pathways where the C–O bonds are fragmented due to the marked antibonding planes across them and give rise to O^- signals.

In sum, the three higher-energy resonances produced by our calculations are seen to involve particularly large

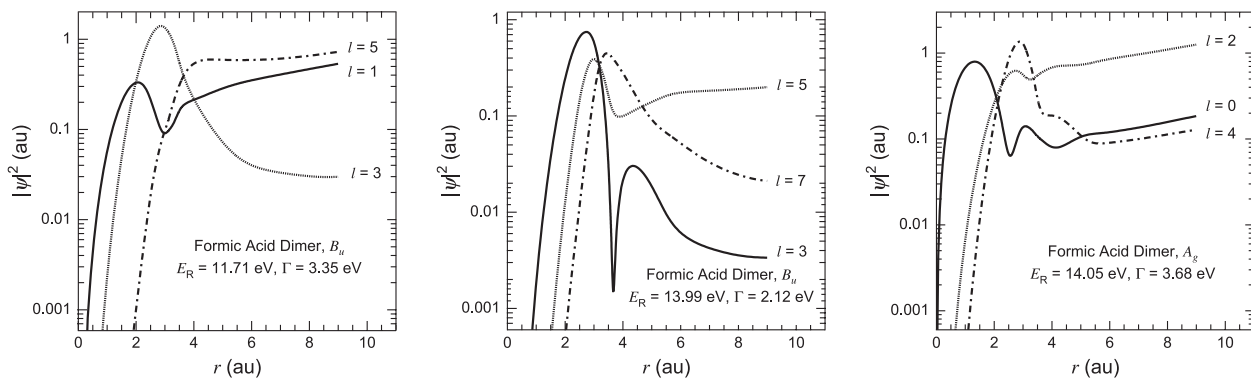


Fig. 10. Radial components of the three resonant wave functions associated to the TNI states at higher energies. Left panel: B_u resonance at 11.71 eV. Center panel: B_u resonance at 13.99 eV. Right panel: A_g resonance at 14.05 eV.

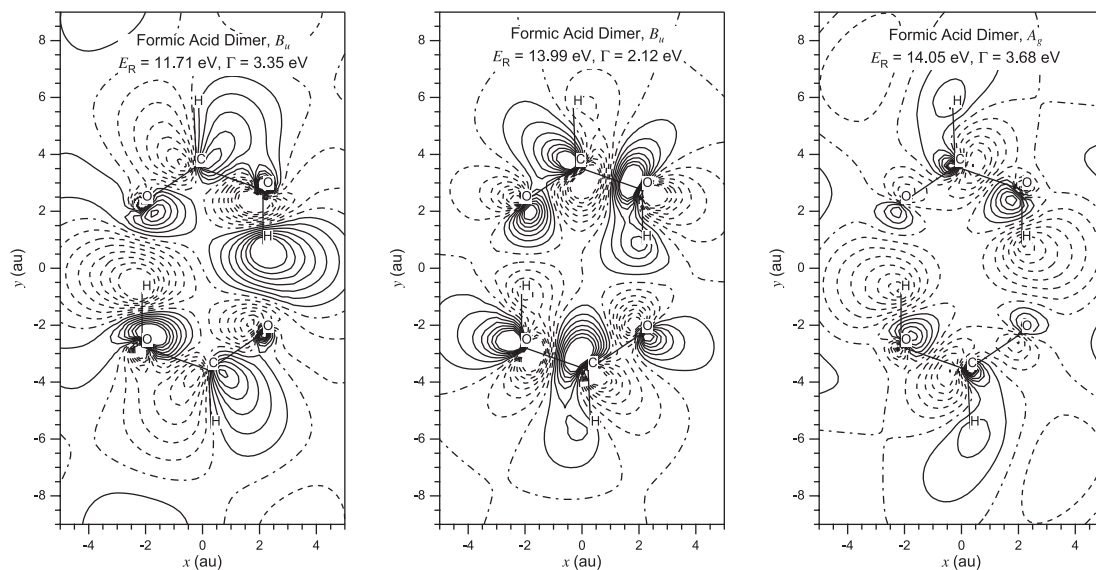


Fig. 11. Isolines describing the spatial mapping of three resonant wave functions plotted in the plane of the FAD. See text for details.

angular momenta in their trapping potentials and to also show strong non adiabatic couplings within them that will contribute to the spatial features of the ensuing TNI states and explain the presence of a complicated structure of antibonding planes in the excess electron density distributions. As a result, one could expect that such states would dissociate by producing a greater variety of smaller fragments (e.g. CO_2^- and O^-) than the resonant states observed at lower energies and as experimentally found [10].

One should also note here that the formic is said to present a π^* resonance from the $\text{C}=\text{O}$ bond around 1.8 eV [22] which should split to two similar resonances at higher and lower energy once one moves to FAD. Our A_u and B_g resonances are both of π^* -type and result shifted to two different energies which are close to the position of the FA single resonance mentioned by [22].

Another interesting feature which allows us to compare the FAD behavior with that of the FA target is to compute total, elastic cross-sections (rotationally summed) for both systems. Our present calculations are given by Figure 12,

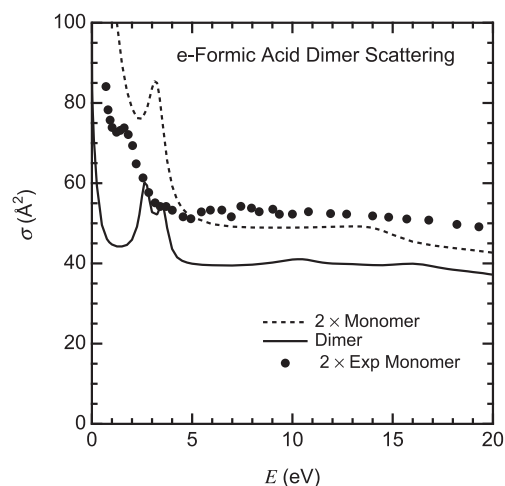


Fig. 12. Computed, integral, elastic total cross-sections (rotationally summed) for the FA monomer multiplied by two (dashes) and the FA dimer (solid line). The black dots are twice the experimental data from reference [23].

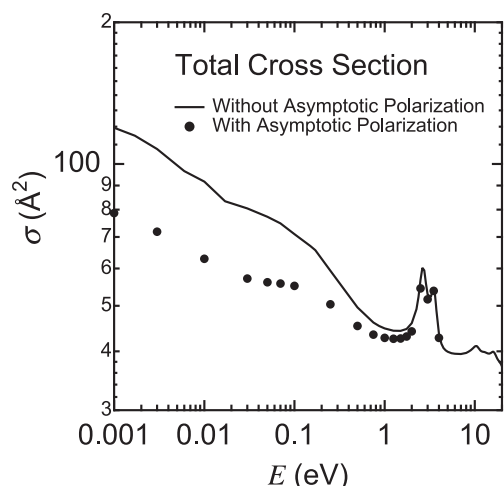


Fig. 13. Computed total cross-sections for the FAD molecule with and without polarisation contributions. The actual spherical polarisability value was $44.97 a_0^3$.

where the experiments from reference [22] are also given for comparison.

One clearly sees that both targets show prominent resonances below 4 eV, with the dimer indicating more of them. Furthermore, the high energy calculations of the dimer show two, well separated, broad resonance regions, while the monomer presents only one of them. Finally, the polar nature of the monomer causes larger threshold cross-sections, as expected within the present body-fixed treatment.

It is also interesting to note that the experimental total cross-sections are very closely followed by our calculations, apart from their very-low-energy behavior where the calculated data shift the experimental resonance to higher energy. We expect this discrepancy to be chiefly due to our lack of exact short-range exchange and correlation effects that are instead modelled from DFT global treatment as discussed before, and therefore to affect calculations in the very low energy domain of the total cross-section. However, considering the complexity of the FAD target, the agreement found here is certainly reassuring as to the general reliability of our present model. We also repeated the calculations from about 4 eV of energy by including long-range polarisation but found no differences in the final cross-sections unless we went down to below about 1.0 eV. The actual calculations down to 10^{-3} eV are shown by Figure 13.

5 Conclusions

We have carried out scattering calculations for the FA dimer kept at its equilibrium geometry and have found that this system presents more resonances than was the case for the FA calculations [12]. The presence of a more complicated pattern of fragmentation, following the formation of more TNI structures, is also confirmed by the experimental studies of both FA clusters [13] and of FA deposited as a film on an Au substrate [10], which show the

increased complexity of the “condensed phase” FA spectra with respect to the findings for the simpler monomer [11].

The results from our scattering calculations indicate three main differences with the previous findings for the FA monomer spectra [11]:

1. the low-energy resonances experimentally shown by Figure 1 are associated with the presence of the $(\text{FAD})^-$ and $(\text{FAD-H})^-$ fragments and the earlier data [13] report also further break-up fragments as $(\text{FA})^-$ and $(\text{FA})(\text{FA-H})^-$. The calculations allow us to locate three low-energy resonances from threshold and up to below 4 eV (two of which are of π^* character) which exhibit realistic widths and spatial features for the excess electron density distributions. They point to the FAD anion formation and also to H abstraction and to dimer break-up as likely decay channels;
2. the presence of a marked resonance with a broader width than those discussed above and located around 9 eV (as experimentally observed), indicating angular momentum couplings which can lead to H^- experimental detection and to cluster dimer break-up, as is in fact observed [13];
3. the existence of further fragmentation patterns at higher energies (up to 15 or 20 eV) where the detected TNIs are O^- and CO_2^- over a very broad range of energies. Our calculations indeed locate three high-energy resonances (in the 11 to 15 eV range) where the numerous contributing angular momenta show complicated antibonding character across several bonds and therefore can provide suitable precursor states for the formation of smaller anionic fragments as CO_2^- and O^- .

In conclusion, in spite of the relative simplicity of the present model, the quantum scattering calculations are indeed seen to be capable of explaining, in semi-quantitative fashion, all the observed experimental findings for target systems where the FAD species discussed here is very likely to play an important role.

One cannot extract from the present calculations the presence of Feshbach resonances, either related to nuclear virtual excitation channels or to virtual electronic excitations, and therefore their possible role cannot be excluded. However, our long experience with the study of trapping resonances in large polyatomic targets has indicated the unexpected role played by unusually large angular momentum barriers, hence of the effects produced by the presence of complicated nodal patterns in the resonant excess electron wavefunctions over the molecular bonding network. This indicates that barrier trapping is a more ubiquitous mechanism than previously thought and that it could easily be coupled to Feshbach-type additional capture.

The financial support of the University of Rome Research Committee and of the CASPUR supercomputing center is gratefully acknowledged. We further thank the EU Research Network EPIC for supporting visits between the cooperating nodes. FAG thanks the Humboldt Stiftung for the award of a Senior Fellowship and RRL thanks the Welch Foundation for financial support under Grant No. A-1020. We also thank for

support the Deutsche Forschungsgemeinschaft (DFG). MS acknowledges funding from the Deutscher Akademischer Austauschdienst (DAAD) through a Ph.D. fellowship and GK acknowledges a visiting fellowship from the European Science Foundation (ESF), action EIPAM (Electron Processing at the Molecular Level), to the Berlin laboratory.

References

1. E.g. see: S. Scheiner, *Hydrogen bonding, A Theoretical Perspective* (Oxford University, New York, 1977)
2. J. Chocholousova, J. Vacek, P. Hobza, *Phys. Chem. Chem. Phys.* **4**, 2119 (2002)
3. F. Madeja, M. Havenith, *J. Chem. Phys.* **117**, 7162 (2002)
4. F. Madeja, M. Havenith, K. Nauta, R.E. Miller, J. Chocholousova, P. Hobza, *J. Chem. Phys.* **120**, 10554 (2004)
5. A. Kohen, J.P. Klinzman, *Chem. Biol.* **6**, R191 (1999)
6. B.J. Bahnson, T.D. Colby, J.K. Chin, B.M. Goldstein, J.P. Klinman, *Prod. Natl. Acad. Sci. USA* **94**, 12797 (1997)
7. W.M. Irvine, P. Friberg, N. Kaifu, Y. Kitamyra, K. Kawaguchi, *Astrophys. J.* **342**, 871 (1989)
8. F. Ban, J.W. Gould, R.J. Boyd, *J. Phys. Chem. A* **104**, 10159 (2000)
9. M.A. Huels, B. Boudaiffa, P. Cloutier, D. Hunting, L. Sanche, *J. Am. Chem. Soc.* **125**, 4467 (2003)
10. T. Sedlacko, R. Balog, A. Lafosse, M. Stano, S. Matejcik, R. Azria, E. Illenberger, *Phys. Chem. Chem. Phys.* **7**, 1 (2003)
11. A. Pelc, W. Sailer, P. Scheier, M. Probst, N.J. Mason, E. Illenberger, T.D. Maerk, *Chem. Phys. Lett.* **362**, 277 (2002)
12. F.A. Gianturco, R.R. Lucchese, *New J. Phys.* **6**, 66 (2004)
13. I. Martin, T. Skalicky, J. Langer, H. Abdoul-Carime, G. Karwasz, E. Illenberger, M. Stano, S. Matejcik, *Phys. Chem. Chem. Phys.* **7**, 2212 (2005)
14. E. Illenberger, *Chem. Rev.* **92**, 1589 (1992)
15. R.R. Lucchese, F.A. Gianturco, *Int. Rev. Phys. Chem. A* **15**, 429 (1996)
16. F.A. Gianturco, A. Jain, *Phys. Rep.* **143**, 347 (1986)
17. E.g. see: *Computational Methods for Electron-Molecule Collisions*, edited by W.M. Huo, F.A. Gianturco (Plenum Press, N.Y., 1995)
18. S.L. Altman, P. Herzig, *Point-Group Theory Tables* (Oxford University Press, Oxford, 1994)
19. S. Hara, *J. Phys. Soc. Jpn* **22**, 710 (1967)
20. J.P. Perdew, A. Zunger, *Phys. Rev. B* **23**, 5048 (1981)
21. F.A. Gianturco, R.R. Lucchese, *J. Chem. Phys.* **111**, 6769 (1999)
22. E.g. see: M. Tronc, M. Allan, F. Edard, *ICPEAC XV Book of Abstracts*, edited by J. Geddes, H.B. Gilbody, A.E. Kingston, C.J. Latimer, H.J.R. Walters (Brighton, 1987), p. 335
23. M. Kimura, O. Sueoka, A. Hamada, Y. Itikawa, *Adv. Chem. Phys.* **111**, 537 (2000)